catalysts

MDPI

Article

Photodegradation under UV Light Irradiation of Various Types and Systems of Organic Pollutants in the Presence of a Performant $BiPO_4$ Photocatalyst

Abdessalam Bouddouch [1,*], Brahim Akhsassi [2,3], Elhassan Amaterz [2], Bahcine Bakiz [2], Aziz Taoufyq [2], Sylvie Villain [3], Frédéric Guinneton [3], Abdelaziz El Aamrani [2], Jean-Raymond Gavarri [3] and Abdeljalil Benlhachemi [2]

[1] Laboratoire de Réactivité et de Chimie des Solides, CNRS-UMR 7314, Université de Picardie Jules Verne, CEDEX 1, 80039 Amiens, France
[2] Laboratoire Matériaux et Environnement (LME), Faculté des Sciences, Université Ibn Zohr, Agadir 80000, Morocco; akhsassibrahim97@gmail.com (B.A.); amaterzhassan@gmail.com (E.A.); bakizlahcen@gmail.com (B.B.); aziz.taoufyq@gmail.com (A.T.); a.amrani@yahoo.fr (A.E.A.); a.benlhachemi@gmail.com (A.B.)
[3] Institut Matériaux Microélectronique et Nanosciences de Provence (IM2NP), CNRS, Université de Toulon, 83000 Toulon, France; sylvie.villain@univ-tln.fr (S.V.); guinneton@univ-tln.fr (F.G.); jean-raymond.gavarri@univ-tln.fr (J.-R.G.)
* Correspondence: abdo.bouddouch@gmail.com

Abstract: In this study, we prepared spheroid microstructures of monoclinic bismuth phosphate $BiPO_4$ by a facile solid-state reaction at 500 °C. The crystal structure was refined using the Rietveld method, where the crystal cell was resolved using a monoclinic system (parameters a, b, c, β) with space group $P2_1/n$. SEM images showed that the solid catalyst presented homogeneous morphologies. These $BiPO_4$ microparticles (BiP-500) have been used as photocatalysts to photodegrade, under UV light irradiation, three cationic dyes (Rhodamine B, RhB; Methylene Blue, MB; and Toluidine Blue, TB), three anionic dyes (Congo Red, CR; Orange G, OG; and Methyl Orange, MO) and mixtures of RhB-MB, RhB-OG and MO-OG organic dyes. The photodegradation efficiency of these BiP-500 microparticles is found to be optimal in the case of RhB solutions, RhB-MB and RhB-OG binary mixtures. The BiP-500 catalyst shows a high selectivity for the conversion of the mixture of dyes into CO_2 and H_2O. Total organic carbon analysis of an anionic dye and a cationic dye (RhB, OG and RhB-MB) confirms the mineralization of the pollutants in the presence of BiP-500 particles. The photocatalytic efficiency of our BiP-500 photocatalyst has been confirmed, with a view to facilitate applications in the field of the depollution of wastewater in the agricultural environment by the degradation of parathion-methyl (PM) as a pollutant.

Keywords: $BiPO_4$; solid-state reaction; photocatalysis; selectivity; parathion-methyl; anionic and cationic dyes

check for updates

Citation: Bouddouch, A.; Akhsassi, B.; Amaterz, E.; Bakiz, B.; Taoufyq, A.; Villain, S.; Guinneton, F.; El Aamrani, A.; Gavarri, J.-R.; Benlhachemi, A. Photodegradation under UV Light Irradiation of Various Types and Systems of Organic Pollutants in the Presence of a Performant $BiPO_4$ Photocatalyst. *Catalysts* **2022**, *12*, 691. https://doi.org/10.3390/catal12070691

Academic Editor: Dehua Xia

Received: 25 May 2022
Accepted: 21 June 2022
Published: 24 June 2022

Publisher's Note: MDPI stays neutral with regard to jurisdictional claims in published maps and institutional affiliations.

1. Introduction

In recent works [1–9], innovative approaches allowing the photodegradation of organic pollutants in aqueous medium using new photocatalysts were described. Indeed, various advanced oxidation techniques for the degradation of gaseous or aqueous pollutants already exist. These techniques are based on the generation of highly reactive hydroxyl and superoxide radicals allowing the destruction of a wide range of pollutants. In particular, heterogeneous photocatalysis involving photonic excitation of semiconductors appears to be a simple, economical and practical method which can totally decompose organic pollutants into H_2O and CO_2 [10,11]. In the process of photocatalysis, the choice of the photocatalyst is important to ensure better efficiency and total degradation. In this sense, in recent years,

several phosphate powders were used as effective photocatalysts in photocatalysis and electrodegradation, such as $BiPO_4$ [12–15], $Cu_2(OH)PO_4$ [16], Ag_3PO_4 [17], $Na_3Bi_2(PO_4)_3$ [18], Na_2MnPO_4F [19], $LiFePO_4$ [20], $ZnS/Zn_3(PO_4)_2$, $4H_2O$ [21], $SrHPO_4$ [22,23], $BaHPO_4$ [24] and $Zn_3(PO_4)_2/ZnO$ [25].

Bismuth phosphate ($BiPO_4$: BiP) is an exceptionally interesting new photocatalyst for the degradation of organic dyes and pesticides, first discussed in 2010 by Pan et al. [12]. BiP is a material recognized as being a valuable analytical reagent used in several applications of catalysis, ion detection, as a material with photoluminescence and catalytic properties [26,27], and can also be used for separate the radioactive elements.

According to the literature, BiP has three polymorphic varieties of crystals [28]. Specifically, it can crystallize in hexagonal phase with space group $P3_121$, and in two monoclinic anhydrous varieties, with space group $P2_1/n$ and space group $P2_1/m$.

Presently, we used the monoclinic phase of $BiPO_4$ (BiP-500) with space group $P2_1/n$, obtained from the solid-state method at 500 °C (see [15]), to photodegrade six anionic and cationic dyes (Rhodamine B, Methylene Blue, Toluidine Blue, Congo Red, Orange G and Methyl Orange), mixtures of dyes and parathion-methyl as a pesticide pollutant. The affinity of the BiP-500 photocatalyst with the two types of dyes was studied and confirmed.

2. Experimental Section

2.1. Sample Preparation

Several methods can be used to synthesize phosphate-based materials in polycrystalline form, such as the low-temperature coprecipitation method in aqueous medium and the high-temperature solid-state method commonly adopted for the elaboration of powder materials. In principle, this high-temperature approach requires a series of grinding and thermal treatments, associated with variations in temperatures and heating times.

The $BiPO_4$ bismuth phosphate was synthesized [15] from bismuth oxide Bi_2O_3 (Fluka Chemika > 99%) and ammonium hydrogen phosphate $(NH_4)H_2PO_4$ (ProLabo $\geq$ 98.0%). Suitable amounts of these starting precursors were ground in an agate mortar and then thermally treated at 500 °C for 3 h.

2.2. Sample Characterization

The identification of the polycrystalline BiP-500 phase was carried out by X-ray diffraction (XRD). The XRD pattern of the polycrystalline sample was recorded at room temperature using an Empyrean Panalytical diffractometer operating at 45 kV/35 mA, using the CuK(α_1–α_2) radiation (λ = 1.5406 and 1.5444 Å) of copper source with Ni filter, and working in continuous mode with a step size of 0.003282°. Scanning electron microscopy (SEM) analysis was used to observe the morphology and the local composition of the crystalline phase. The device used was a Supra 40 VP Column Gemini Zeiss operated at 20 KeV, coupled with an Energy Dispersive X-ray Spectroscopy (EDXS) type analyzer, allowing the determination of the local elemental compositions of our material. To determine the gap energy of the as-synthesized $BiPO_4$, the UV-Vis diffuse reflectance spectrum (DRS) was plotted in the wavelength range from 200 nm to 400 nm, using a Shimadzu type UV-Vis spectrophotometer, UV-2600i, at room temperature.

Fourier transform infrared (FTIR) spectroscopy allowed us to characterize the polycrystalline sample using an IRAffinity-1S SHIMADZU spectrometer, equipped with a Jasco ATR PRO ONE module, in the wavenumber range from 400 to 4000 cm^{-1}, with a resolution of 4 cm^{-1}. The samples were packaged as a dispersion in a pellet comprising 1 wt % of $BiPO_4$ mixed and ground with 99 wt % KBr.

2.3. Calculation Methods

Electronic structure calculations of $BiPO_4$ ($P2_1/n$) were executed by the QUANTUM ESPRESSO program [29], with exchange and correlation treated by generalized gradient approximation (GGA) with the Perdew–Burke–Ernzerhof (PBE) function [30], using a norm-conserving pseudo potential for the Bi atom and ultra-soft pseudo potentials for P and O

atoms. The atomic configurations of the Bi, P and O atoms are Bi, $[Xe]4f^{14}5d^{10}6s^26p^3$; P, $[Ne]3s^23p^3$; and O, $[He]2s^22p^4$. All calculations were performed with kinetic energy cutoffs of 80 and 720 Ry for wave functions and charge density, respectively, and with a $4 \times 4 \times 4$ as Monkhorst−Pack k-point [31]. The geometry of $BiPO_4$ (Figure 1) was optimized by the Broyden–Fletcher–Goldfarb–Shanno (BFGS) method on a $P2_1/n$ monoclinic unit cell (a = 6.7553(1) Å, b = 6.9419(1) Å, c = 6.4772(1) Å and β = 103.690(1)°), using 14 μeV/atom as the total energy convergence.

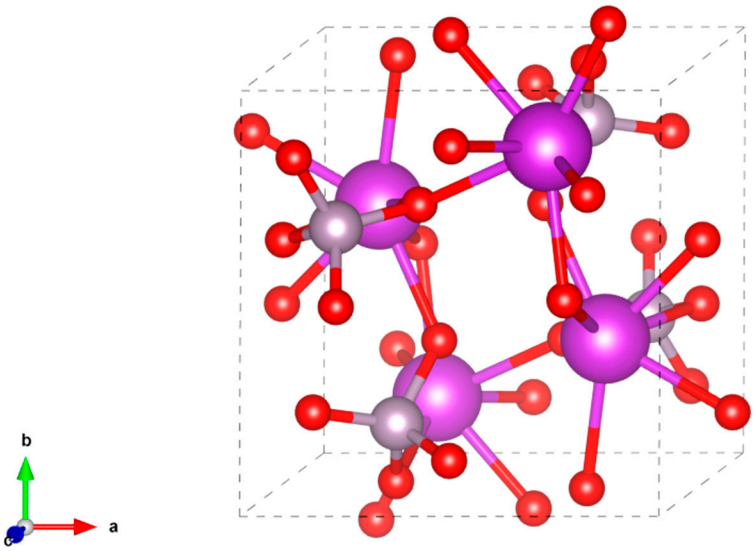

Figure 1. Bulk crystal structure of BiP-500. Purple, gray and red balls represent Bi, P and O atoms, respectively.

2.4. Photocatalytic Experiments

The UV degradation reactor used in this work consisted of a cubic-shaped geometry with 5 low-pressure mercury lamps (Osram, PURITEC HNS Germicidal Lamps G23), each at a nominal power of 7 w and 1.8 w for radiated power $200 \leq \lambda \leq 280$ nm (UV-C) with a distance of 20 cm above the beaker, which contains the catalyst with the pollutant. The UV intensity at a wavelength of 253.4 nm of each lamp is of the order of 0.140 w m^{-2}. A cooling system was applied to avoid the effect of temperature. The temperature of the solution was maintained between 26 °C and 28 °C. The homogeneity of the solution was ensured by a magnetic stirrer. The different photocatalytic activities under UV light irradiation of BiP-500 particles in aqueous medium were evaluated by the analyses of photodegradation as a function of irradiation time of three cationic dyes (Rhodamine B, Methylene Blue and Toluidine Blue), three anionic dyes (Congo Red, Orange G and Methyl Orange), mixtures of these dyes and parathion-methyl. A fixed mass of 100 mg of photocatalyst was suspended in 100 mL of dye solution (with a fixed concentration of 5 mg L^{-1}). Before irradiation, the solution was stirred for 1 h inside the reactor in the dark to obtain the adsorption–desorption equilibrium between the support and pollutant. During irradiation, 3 mL solution was collected every 2 min of irradiation. UV-Vis JENWAY-6705 spectrometry was used to determine the concentration of the pollutant as a function of irradiation time.

2.5. Point of Zero Charge Determination

The point of zero charge pH_{pzc} is defined as the pH value for which the surface charge is equal to zero, namely, the pH at which the charge due to the positive surface groups is equal to that due to the negative ones. The pHpzc of the BiP-500 surface was determined following the method described by Al-Harahsheh [32]: 50 mg catalyst was added into six beakers containing 50 mL of 0.1 M potassium nitrate solution. The initial pH values (pHi) of these solutions were adjusted to 2, 4.01, 6.25, 8.21, 10.03 and 12.02 by adding a few drops of either 0.1 M sodium hydroxide (NaOH) or 0.1 M nitric acid (HNO_3). The solution

was equilibrated for 48 h. The suspension was then filtered, and the final pH values (pHf) of these solutions were determined.

2.6. Total Organic Carbon Analysis

The mineralization of cationic and anionic dyes and their intermediates during the photocatalytic reaction was evaluated by measuring the total organic carbon (TOC) present in aqueous solution. The analysis was performed with a Shimadzu TOC-5000-A system equipped with a non-dispersive infrared detector and an ASI-5000-A auto-sampler. Potassium hydrogen phthalate solutions with known carbon concentrations were used to draw the calibration line. The temperature of the solution was maintained at 25 ± 4 °C.

3. Characterizations of the $BiPO_4$ Photocatalyst

3.1. Structural Studies

The identification of the as-synthesized BiP-500 polycrystalline phase was carried out by X-ray diffraction (see Figure 2a), using the JCPDS file (No. 01-080-0209). To characterize the obtained phase and clearly show the absence of any residual other phase in the powder, Rietveld analysis was performed using FullProf software [33] and introducing the initial atom coordinates obtained from literature data [34]. The standard deviations were multiplied by the Berar factor to correct the local correlations according to J. F. Berar et al. [35]. A very good agreement between observed and calculated XRD profiles was obtained (Figure 2b). Table 1 shows the main results. The calculated cell parameters are in good agreement with literature results:

a(Å) = 6.7553(1), b(Å) = 6.9419(1), c(Å) = 6.4772(1), β(°) = 103.690(1), V(Å^3) = 295.115(8)

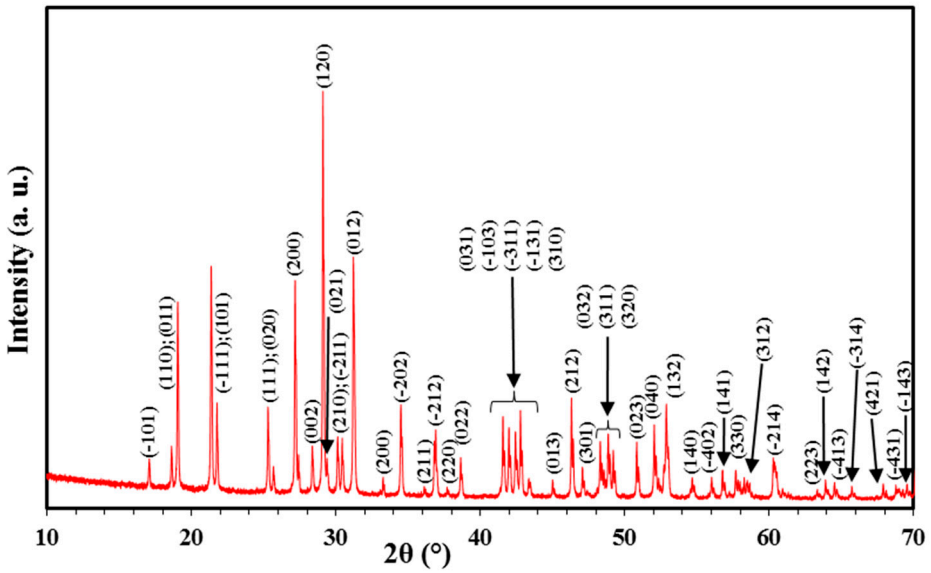

(**a**)

Figure 2. *Cont.*

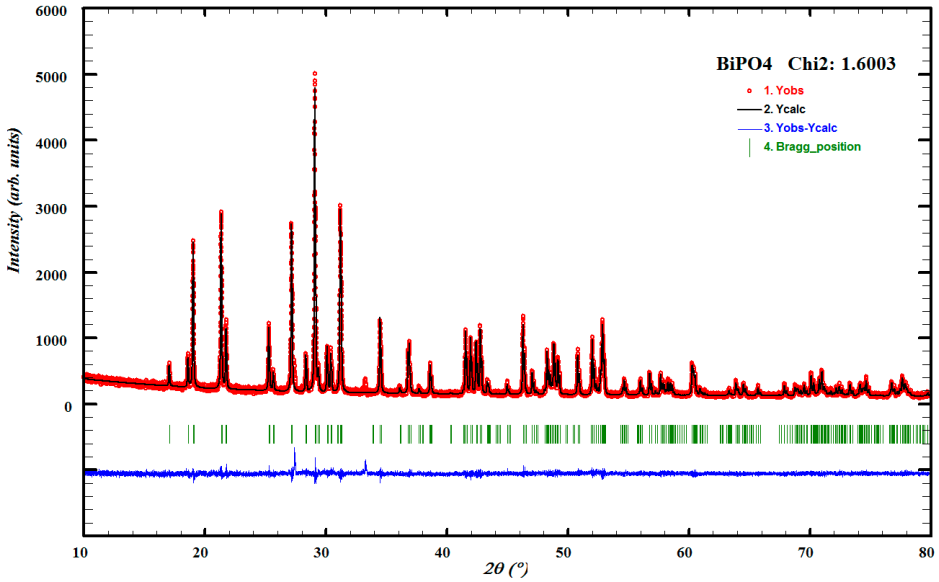

(**b**)

Figure 2. (**a**) XRD pattern of monoclinic $BiPO_4$ (space group $P2_1/n$). (**b**) Results of Rietveld refinement calculations for the monoclinic BiP-500 compound.

Table 1. X-ray diffraction results at 25 °C: Rietveld structure refinement of the $BiPO_4$ phase thermally treated at 500 °C.

Cell Parameters (10^{-10} m) Volume (10^{-30} m) Standard Deviations in Parentheses: ( )	**Lattice System, Space Group**	**Reference JCPDS 80-0209**
a = 6.7553(1)	Monoclinic $P2_1/n$	a = 6.7626(1)
b = 6.9419(1)		b = 6.9516(1)
c = 6.4772(1)		c = 6.4822(8)
β = 103.690(1)		β = 103.736(1)
V = 295.115(8)		V = 296.018(8)
$R_B = 100.\{\sum \lvert I_k^{obs} - I_{ki}^{calc} \rvert / \sum \lvert I_k^{obs} \rvert\}$		=3.5%
$R_F = 100.\{\sum \lvert F_k^{obs} - F_{ki}^{calc} \rvert / \sum \lvert F_k^{obs} \rvert\}$		=2.9%
$R_p = 100.\{\sum \lvert y_i^{obs} - y_i^{calc} \rvert / \sum \lvert y_i^{obs} \rvert\}$		=5.5%
$R_{wp} = 100.\{\lvert \sum w_i \lvert y_i^{obs} - y_i^{calc} \rvert 2 / \sum w_i \lvert y_i^{obs} \rvert 2]^{1/2}\}$		=7.7%
$R_{exp} = 100.\{[(N - P + C) / \sum w_i \lvert y_i^{obs} \rvert 2]^{1/2}\}$		=6.2%
Where N, P and C are the number of observations, parameters and constraints, respectively.		
Atom (Wyckoff)	x	y	z	B_{iso} (Å^2) (*)
Bi	0.2855(3)	0.1453(3)	0.0864(3)	0.56(5)
P	0.296(2)	0.161(2)	0.615(2)	0.84(27)
O_1	0.263(3)	−0.002(2)	0.438(3)	0.33(67)
O_2	0.377(3)	0.344(4)	0.515(3)	1.24(65)
O_3	0.458(3)	0.105(3)	0.815(3)	1.13(68)
O_4	0.115(3)	0.198(3)	0.709(3)	1.37(72)

(*) Note: Isotropic Debye–Waller thermal factor: $B = (8\pi^2/3) \langle R^2 \rangle$ with R associated with vibration amplitudes of atoms.

The calculated full width at half maximum (FWHM) of Bragg peaks confirmed the high level of crystallization of this as-prepared BiP-500 sample (this can be easily evidenced from the observation of the separation of $K\alpha_1$–$K\alpha_2$ doublets in Bragg peal profiles). Figure 2b shows that no additional phase is observed.

3.2. Scanning Electron Microscopy

Scanning electron microscopy images associated with local chemical EDX analyses are shown in Figure 3a–c. A spheroid morphology is observed and the linear dimensions D of these BiP-500 particles range between 200 and 300 nm (<D> = 250 (±50) nm). This confirms the high level of crystallization observed in our XRD analyses (see Section 3.1).

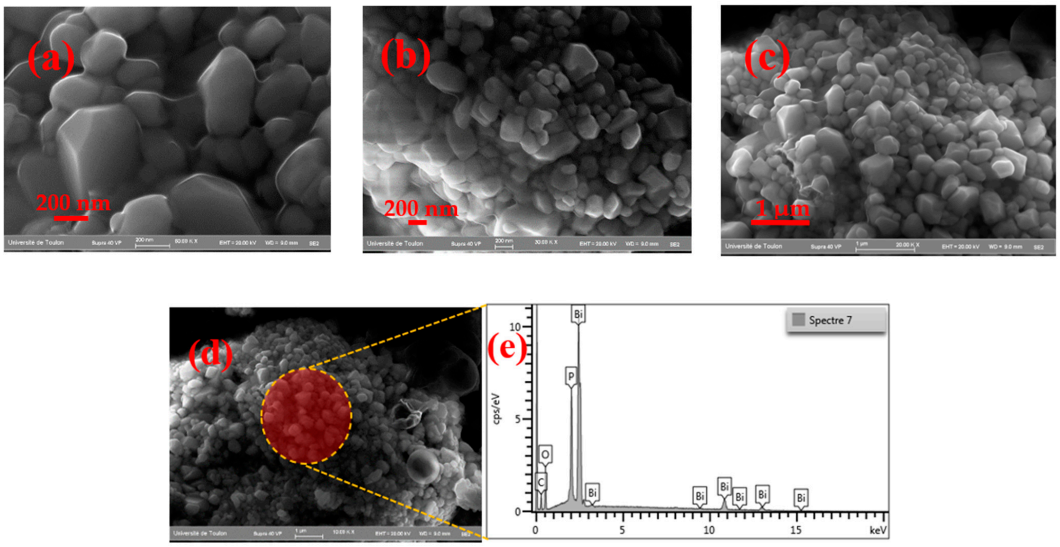

Figure 3. SEM images and EDX spectrum of $BiPO_4$ treated at 500 °C.

The EDX analysis of the red zone in Figure 3d is given in Figure 3e—the presence of the three elements Bi, P and O is confirmed, with an atomic ratio of Bi/P (49.5/50.5) close to 1.

3.3. FT-IR Spectroscopy Analyses

The FTIR spectrum of the as-synthesized BiP-500 sample (Figure 4) is composed of different bands. The $[PO_4]$ group is characterized by two types of vibration modes in the range 450–650 cm^{-1} and 900–1100 cm^{-1} [34,36–39]. Based on previous studies on phosphate, the 1072, 1001 and 954 cm^{-1} observed bands can be assigned to the asymmetric stretching vibration ν_3 of the P–O bonds, and the 925 cm^{-1} observed band can be assigned to the corresponding ν_1 symmetric vibration. The bending vibration modes of O–P–O bonds are observed around 615, 557, 549 and 526 cm^{-1}.

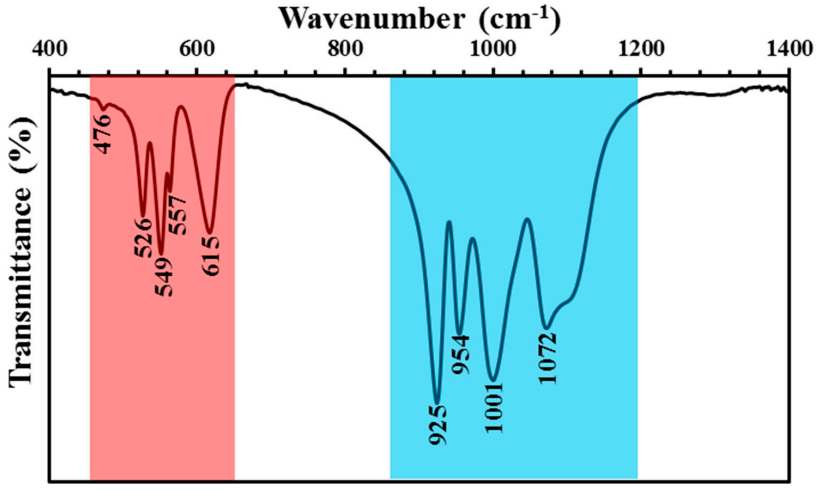

Figure 4. FT-IR spectroscopy of BiP-500: vibrational bands and wavenumbers in cm^{-1}.

3.4. UV-Vis Diffuse Reflectance Spectroscopy

Diffuse reflectance surface (DRS) analysis was performed to investigate the optical absorption properties of as-synthesized BiP-500 phase. As shown in Figure 5, BiP-500 has a broad band gap with excellent optical absorption in the range of 260 nm to 350 nm. Therefore, BiP-500 can only be excited by UV irradiations with wavelengths lower than 260 nm. The band gap energy (E_g) was calculated according to Tauc's formula $(\alpha \cdot h\nu)^{1/\gamma} = B(h\nu - E_g)$ [40], where α is the absorption coefficient, h is the Planck constant, ν is the photon's frequency and γ is the factor depending on the type of band gap of the semiconductor—it can be equal to 1/2 or 2 for direct or indirect band gaps, respectively. Based on the literature, the monoclinic $BiPO_4$ has an indirect transition band gap ($\gamma = 2$) [41]. Hence, the value $E_g = 4.38$ eV was finally obtained from the plot of $(\alpha \cdot h\nu)^{1/2}$ vs. $h\nu$ (Figure 5). This energy value agrees with that of other works [32] on the monoclinic phase (P21/n, noted nMBIP).

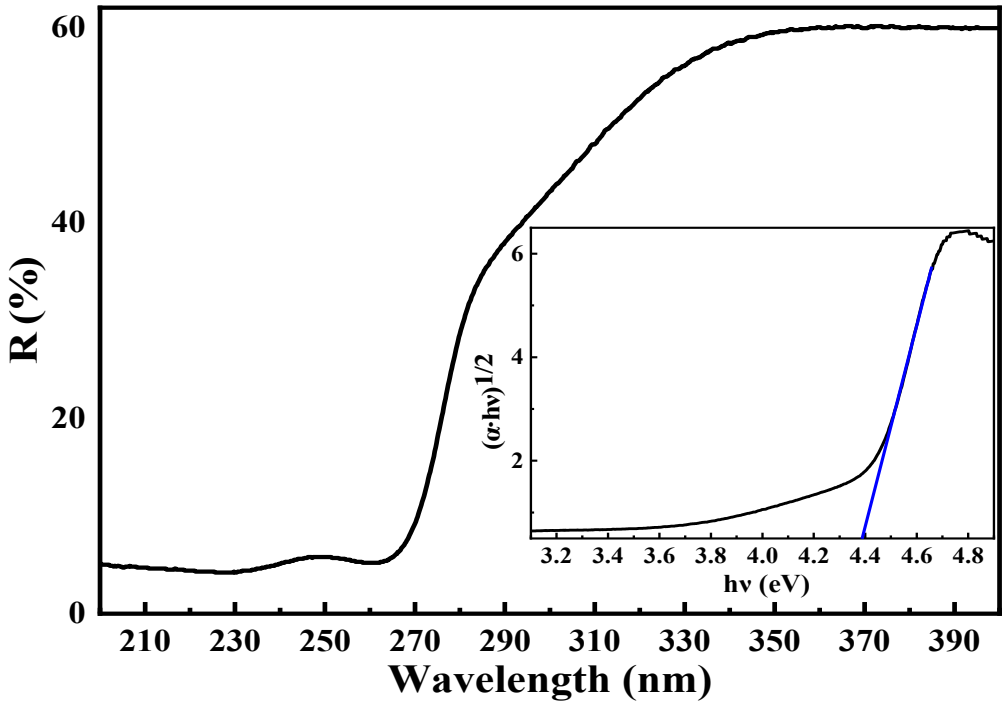

Figure 5. UV-Vis diffuse reflectance of BiP-500 with inset of the band gap energy obtained by Tauc's plot (indirect band gap).

3.5. Density Functional Theory Calculations Results

To deeply investigate the photocatalytic degradation mechanism, band gap, total density of states (TDOS) and partial density of states (PDOS) were implemented on the optimized bulk structure of $BiPO_4$ (space group $P2_1/n$). As presented in Figure 6, $BiPO_4$ is an n-type semiconductor with an indirect band gap, with the conduction band minimum (CBM) and valence band maximum (VBM) located at the k-points of D and Γ, respectively. It has a wide band gap of 4.45 eV along the high symmetry directions. This energy value is estimated to be 0.07 eV or 1.6% compared to the experimental one, E_g 4.38; however, it is in good agreement with other theoretical band gaps [42]. TDOS and PDOS are shown in Figure 7a,b, revealing the greatest intensity in the curves, which could be interpreted by the greater generation of the electrons at the surface of $BiPO_4$, consequently producing more reactive oxidizing species during the photocatalytic reactions. Based on the PDOS in the −8 to 12 eV region, it is possible to identify the states contributing to the photocatalytic activities. The valence band maximum of $BiPO_4$ (VBM) is mainly composed of O (2p), and some contribution from Bi (6s) and Bi (6p) states. The other conduction band minimum (CBM) is composed of Bi (6p) (Figure 7b).

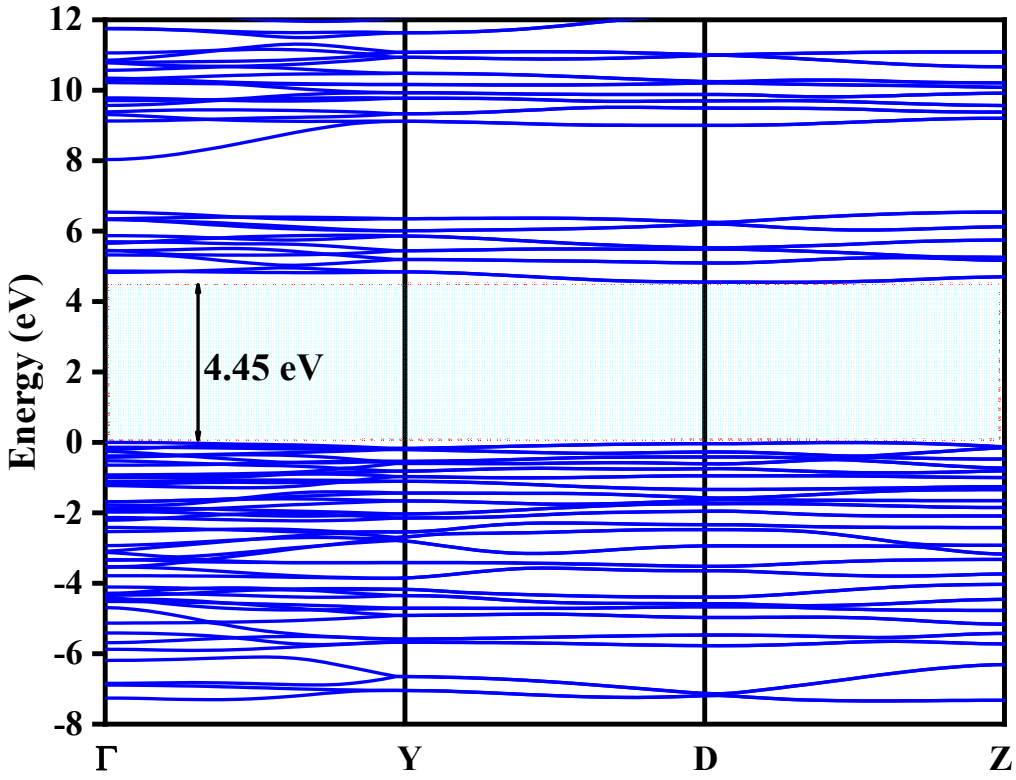

Figure 6. Band structure of bulk BiP-500. The fermi level is set to 0.

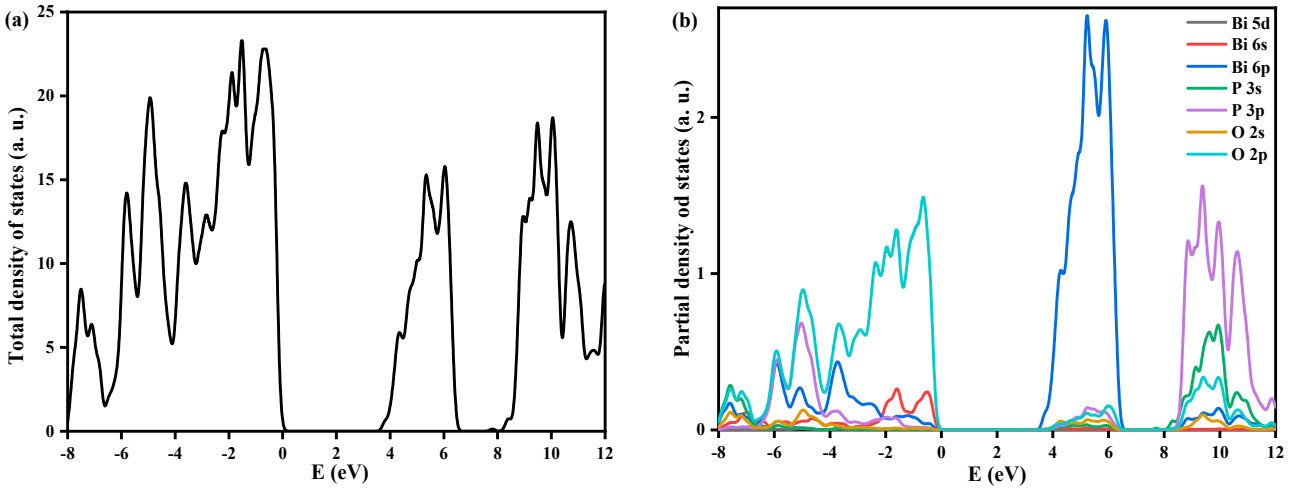

Figure 7. (**a**) Total density of states TDOS and (**b**) partial density of states PDOS of BiP-500. The fermi level is set to zero.

4. Evaluation of the Photocatalytic Activity of BiP-500

4.1. Photolysis and Adsorption Test of BiP-500

In order to show the efficiency of our BiP-500 photocatalyst, it is essential to characterize the direct adsorption of the pollutant in the absence of UV-Vis light. The photolysis test allows the determination of the photocatalytic degradation contribution under our operating conditions. In this sense, we carried out a preliminary study to verify the part of adsorption and photolysis of pollutants (case of RhB).

Figure 8a shows the absorption spectra of rhodamine (B) in the presence of BiP-500. It is noted that the decrease in intensity of the maximum absorption band of RhB does not exceed 5.1% after 5 h of contact, which corresponds to a very weak adsorption of RhB by the photocatalyst BiP-500.

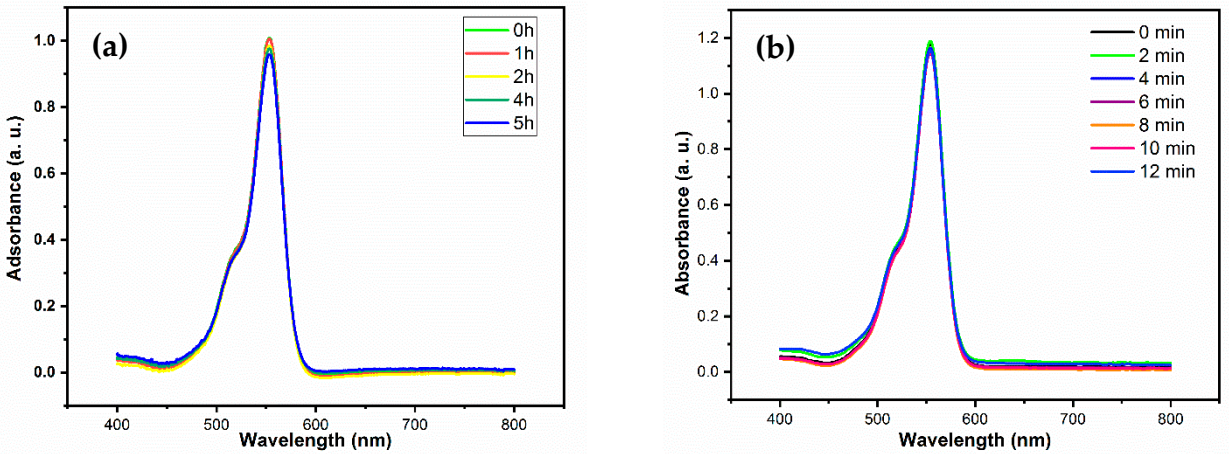

Figure 8. (**a**) Absorption spectrum of RhB in the presence of BiP particles and in the absence of UV irradiation; (**b**) photocatalytic degradation of RhB dye under UV light irradiation in the absence of the catalyst.

On the other hand, the distribution of the particles presented in Figure 9 and the areal parameters illustrated in Table 2 show that BiP-500 is characterized by a specific surface of the order of 3.52 m^2/g, in good agreement with the measurements found in the literature. This is well correlated with the very low adsorption capacity of this material in the presence of the organic pollutant and in the absence of UV-Vis irradiation.

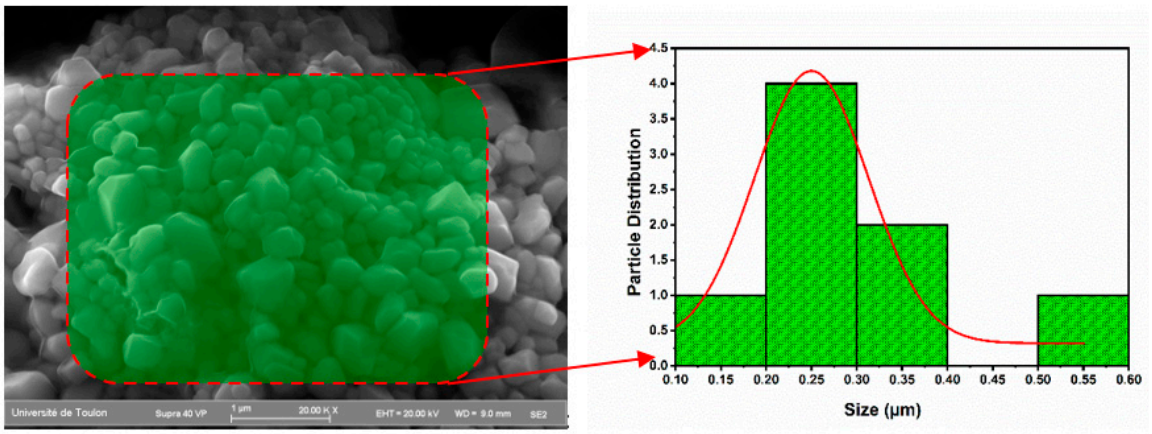

Figure 9. Distributions of particle sizes of BiP-500 photocatalyst.

Table 2. Areal parameters of the BiP-500 catalyst.

Areal Parameters of the BiP-500 Catalyst	
Mass of photocatalyst (in mg)	100
Crystallite size D in nm	250
Exposed surface Sexp (m^2)	0.35
SSA (m^2/g)	3.52
-Specific surface areas of crystallites in the form of a sphere: Exposed surface: Sexp = (6/D)(m/µ); specific surface area: SSA = (6/Dµ); m = total mass of photocatalyst; µ = theoretical density of the material from crystallographic data.	

The direct photolysis test (in the absence of the photocatalyst) was carried out on a solution (RhB) with an initial concentration of 5 mg L^{-1} under UV-Vis irradiation.

Figure 8b shows that in the absence of the BiP-500 photocatalyst, only a degradation of 2 (±1)% of the RhB is obtained after 12 min of irradiation. These results agree with the

results in the literature on the degradation of rhodamine B by direct photolysis and with UV-Vis irradiation at λ = 254 nm.

Given these results, it can be concluded that the process responsible for the degradation of the organic pollutants in the presence of the photocatalyst BiP-500 will be, essentially, the photocatalytic photodegradation, and not the adsorption and direct photolysis.

4.2. Photodegradation of Various Organic Dyes

The photocatalytic performances of the BiP-500 particles were evaluated by determining the photodegradation as a function of the irradiation time of different organic dyes (cationic and anionic) in an aqueous solution, under UV light irradiation.

The aqueous solutions of the organic dyes (5 ppm) of RhB, MB, TB, MO, CR and OG, with a concentration of 5 mg L^{-1} (5 ppm), were prepared by dissolving the analytical-grade dye in distilled water. In each dye solution (5 ppm), particles of BiP-500 were dispersed with a fixed concentration of 1.0 g L^{-1}, at room temperature.

Before any irradiation, each solution was stirred magnetically for one hour in the dark to establish the adsorption–desorption equilibrium. Under irradiation and in the absence of BiP-500 photocatalysts, very weak degradation of the various dyes occurred, indicating a high stability of these molecules.

The photodegradation process was analyzed by measuring the intensity of the different absorption bands at well-determined wavelengths: 554, 663, 630, 450, 498 and 481 nm for Rhodamine B (RhB), Methylene Blue, Toluidine Blue, Methyl Orange, Congo Red and Orange G, respectively. Each absorption band intensity was assumed to be proportional to the concentration of the pollutant.

The mixed suspensions (pollutant + BiP-500) were irradiated with 5 × 7 W UV-Vis lamps (λ = 254.7 nm). Every 2 min, 3 mL aliquot was taken out; the suspension was removed by centrifugation before determining the concentration of residual dye by UV-Vis spectrophotometry.

The efficiency of photodegradation was determined via the C_t/C_0 ratios (Equation (1)), where Ct and C_0 are the concentrations of BiP-500 particles at times t and t = 0. The nature of kinetics was analyzed through the relation:

$$\ln(C_t/C_0) = -k_{obs}\, t \quad (1)$$

In this relation, the apparent kinetics constant k_{obs} would characterize a behavior corresponding to a first-order kinetics rate law (Langmuir–Hinshelwood model).

Figure 10 shows that the various intensities of UV-Vis absorption spectra of the solutions of dyes decrease as a function of irradiation time. This indicates that the decreasing concentrations of dyes C_t (RhB, MB, TB, CR, OG and MO) are directly due to photocatalytic degradation.

Figure 11a gathers the six C_t/C_0 curves obtained from the various UV-Vis absorption spectra. The results show that the photocatalytic activities of the cationic dyes RhB, MB and TB are higher than those of the anionic dyes MO, RC and OG.

Figure 11b represents the variations in ln (C_0/C_t) as a function of the irradiation time (t). A linear correlation between ln (C_0/C_t) and t can be clearly observed for all pollutants. The various rate constants k_{obs} for the photodegradation of RhB, MB, TB, CR, OG and MO dyes are 0.289 (±0.003), 0.179 (±0.009), 0.148 (±0.005, 0.122 (±0.005), 0.111 (±0.0004) and 0.063 (±0.005) min^{-1}, respectively.

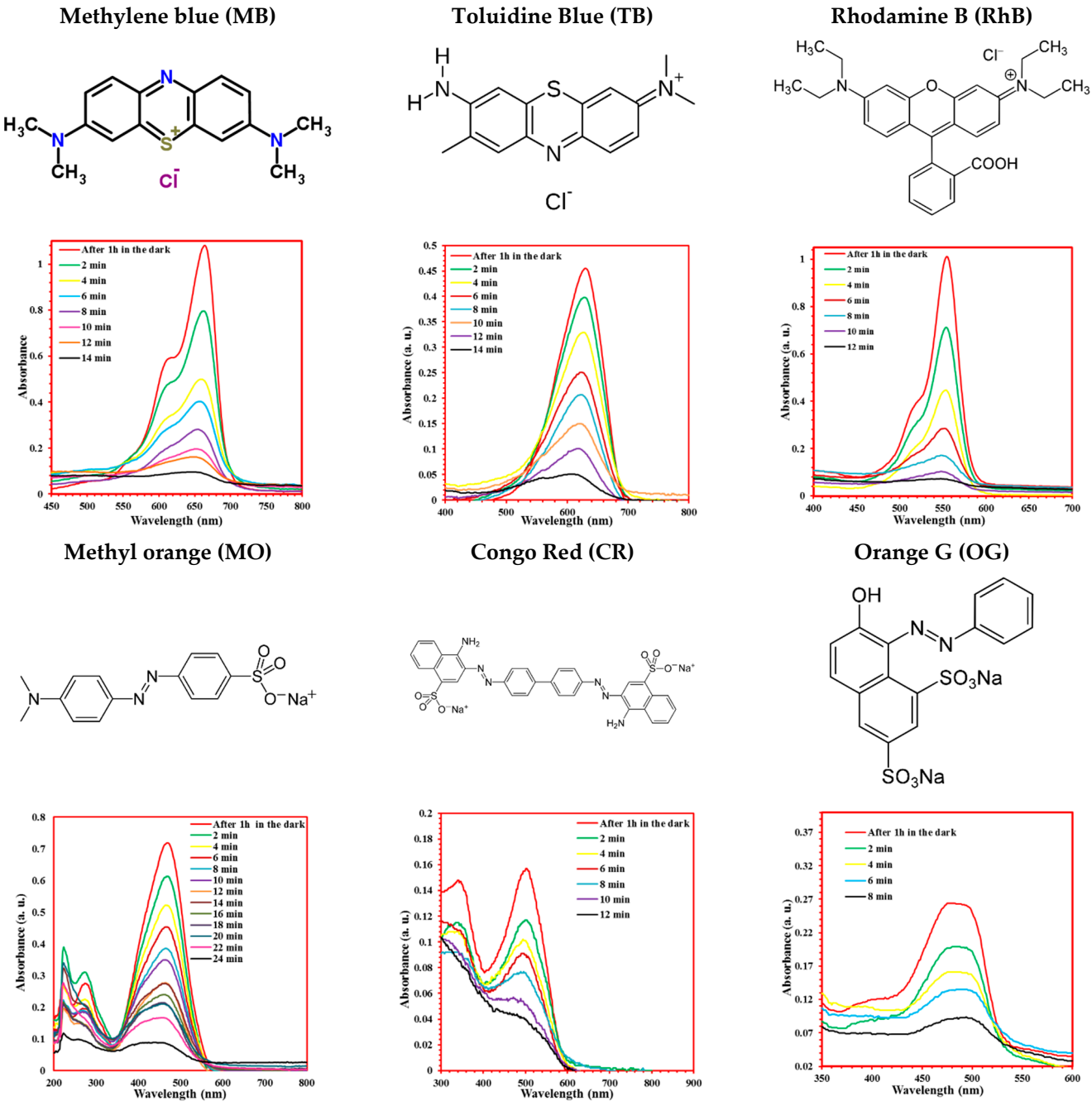

Figure 10. UV-Vis absorption with time irradiation of a solution containing 100 mg of BiP and 5 ppm of pollutants (MB, TB, RhB, MO, CR, OG).

This result indicates that the photocatalytic efficiency of the BiP-500 particles appears the highest in the case of the photodegradation of the RhB dye (Figure 11c). It is also noted that for the photodegradation of this RhB dye, the photocatalytic activity of the BiP-500 phase is greater than that of the BiP-400 and BiP-600 phases in our previous work [14] (these phases were synthesized by the coprecipitation method followed by thermal decomposition at 400 °C and 600 °C, respectively).

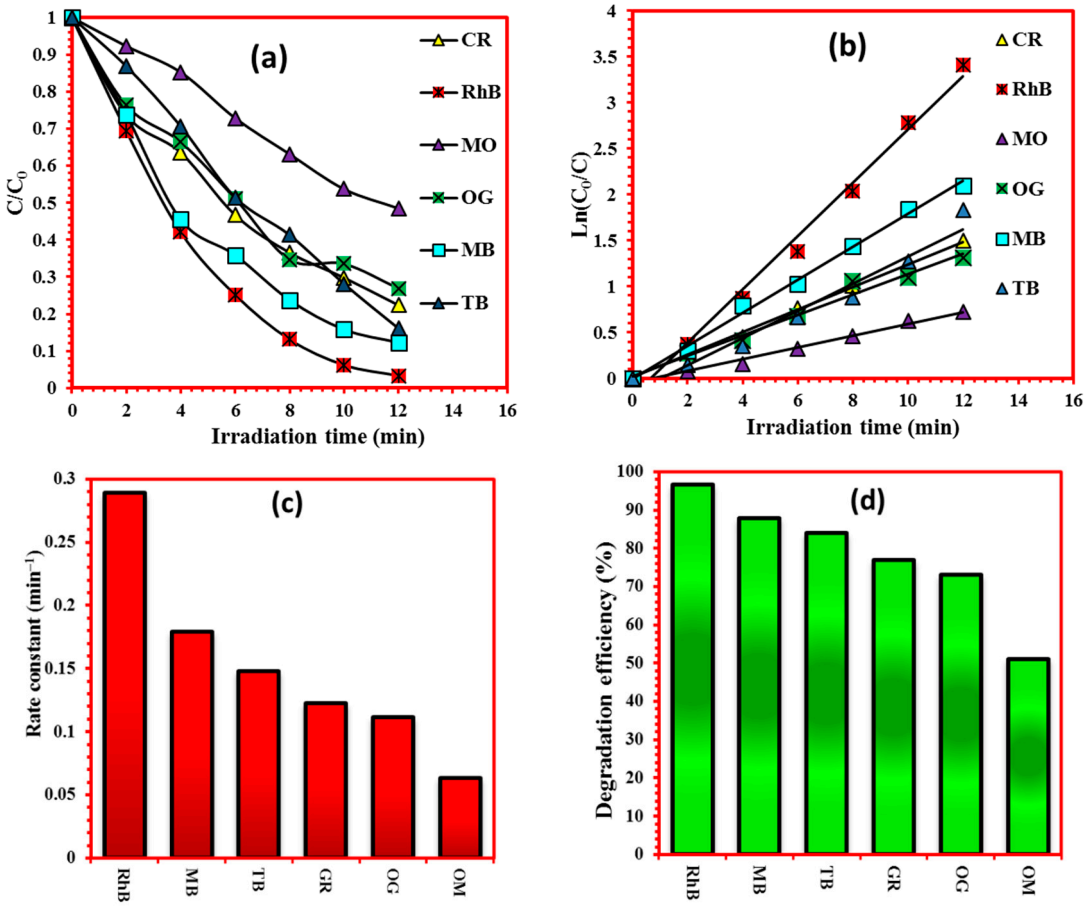

Figure 11. (**a**) Variation in C_t/C_0 ratio as a function of time for the different pollutants (RhB, MB, TB, GR, OG, OM); (**b**) pseudo-first-order kinetics of the photodegradation mechanism for all pollutants; (**c**) evolution of the associated apparent rate constant k_{obs} as a function of pollutants; (**d**) efficiency of degradation after irradiation time of 12 min for the degradation of different pollutants.

After 12 min of irradiation under UV, the elimination rates for the RhB, MB, TB, CR, OG and MO dyes are 96.7%, 87.8, 84%, 77%, 73% and 51%, respectively (Figure 11d). Figure 11d shows that the least degraded OM dye, however, reaches a degradation rate of 50% in the presence of this BiP-500 photocatalyst.

To better understand the high photodegradation efficiency observed in the case of cationic dyes compared to anionic dyes, we determined the pH at the point of zero charge, pH_{pzc} (Figure 12). The effect of the pH of solution on photodegradation is related to the acid–base property of the semiconductor surface (Bi-O-) that can be characterized by the determination of the point of zero charge [17,43–45]. Figure 10 shows the graph reporting the difference (pHf–pHi) as a function of pHi. The pH_{pzc} of BiP-500 corresponds to the specific aqueous solution for which pH_f = pHi; this pH_{zpc} is of the order of 4.01. At pHi values either below or above pH_{zpc}, the BiP-500 surface charge is either positive or negative, respectively. In other words, the surfaces of BiP-500 particles can be negatively or positively charged depending on the pH of the environment (Equations (2) and (3)). The corresponding reactions can be expected as follows:

$$pH < pH_{pzc}\ BiPO_4\text{: Bi-OH} + H^+ \rightarrow BiOH_2{}^+ \quad (2)$$

$$pH > pH_{pzc}\ BiPO_4\text{: Bi-OH} + OH^- \rightarrow BiO^- + H_2O \quad (3)$$

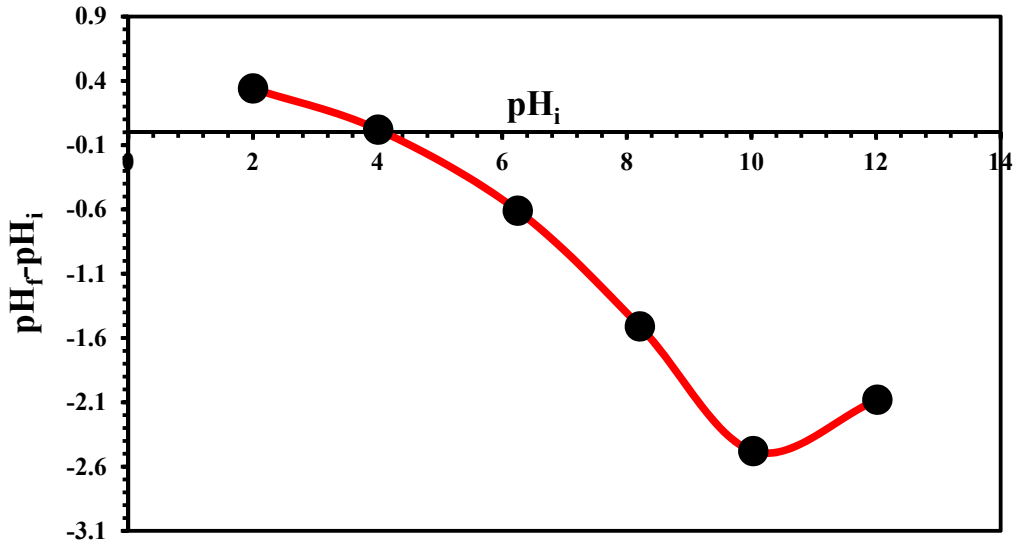

Figure 12. Determination of the point of zero charge of BiP-500 photocatalyst: pH_{pzc} = 4.01.

4.3. Photodegradation of Dyes Mixtures

The different photocatalytic performances of the BiP-500 particles were tested in the cases of photodegradation of mixtures of cationic–cationic (RhB and MB), cationic–anionic (RhB and OG) and anionic–anionic (MO and OG) dyes. The photodegradation experiments of the solutions of each mixture under UV-Vis irradiation were carried out for 14 min with samples taken every 2 min. In Figure 13a–c, all binary solutions ((a) RhB-BM, (b) RhB-OG and (c) MO-OG) show a decrease in absorption bands as a function of time in the presence of BiP-500. The complete disappearance of the absorption bands was obtained after 14 min of irradiation for the three mixtures. This new experimental approach involving dye mixtures could be of value in the depollution of real wastewater, using a non-toxic photocatalyst.

Table 3 shows the photocatalytic efficiency of $BiPO_4$-based catalysts reported in the literature using several synthesis methods, examined pollutants and irradiation sources. It is clear from the table that the activity of BiP-500 used in this work has been improved towards the degradation of various types and systems of organic pollutants compared to other catalysts based on $BiPO_4$. The high activity of $BiPO_4$ is due to the high separation of the electron–hole pair during the photocatalytic illumination.

Table 3. Comparison of the photocatalytic activity of the BiP-500 catalyst with other reported photocatalysts.

Catalyst	Pollutant Examined	Synthesis Method	Operating Conditions (C_0; Light Source)	Degradation Efficiency; Time	Ref.
$BiPO_4$	RhB	Hydrothermal	5 ppm, UV 254 nm	k_{app} = 0.1225 min^{-1}, 30 min	[46]
$BiPO_4$	RhB	Solvothermal	5 ppm, UV 254 nm	k_{app} = 0.53 h^{-1}, 180 min	[47]
$BiPO_4$	MO	Microwave	10 ppm, 500 W Xe lamp	k_{app} =0.035 min^{-1}	[48]
$BiPO_4$	MB	Coprecipitation	15 ppm, UV 254 nm	k_{app} = 0.1089 min^{-1}	[49]
$BiPO_4$	MB	Flux	5 ppm, UV 254 nm	k_{app} = 0.193 min^{-1}	[50]
$BiPO_4$	RhB	Coprecipitation	5 ppm, UV 254 nm	98%, 160 min	[14]
BiP-500	RhB	Solid-state	5 ppm, UV 254 nm	96.7%, 12 min	This study
BiP-500	MB	–	–	87.8%, 12 min	This study
BiP-500	TB	–	–	84%, 12 min	This study
BiP-500	CR	–	–	77%, 12 min	This study
BiP-500	OG	–	–	73%, 12 min	This study
BiP-500	MO	–	–	51%, 12 min	This study
BiP-500	PM	Solid-state	10 ppm, UV 254 nm	93%, 30 min	This study

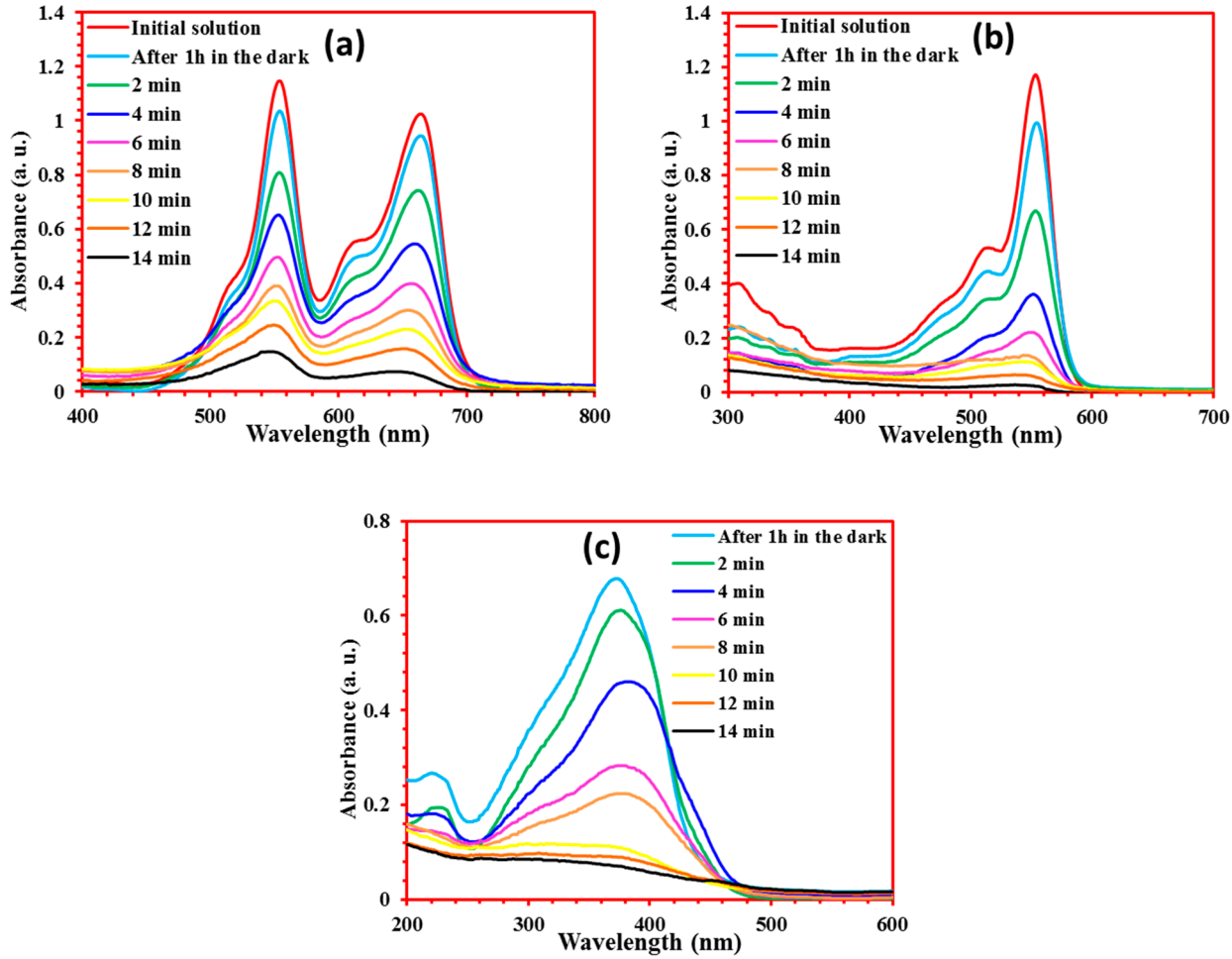

Figure 13. Absorption spectra of a mixture of two dyes photodegraded under UV-Vis light in the presence of BiP-500 photocatalyst: (**a**) RhB + MB, (**b**) RhB + OG and (**c**) MO + OG.

4.4. Mineralization of Pollutants RhB, OG and Mixture Dyes (RhB-MB)

The determination of total organic carbon (TOC) removal can allow us to determine the level of mineralization of pollutants after photocatalysis and constitutes an additional approach of the photocatalytic performance of photocatalysts. Figure 14 shows the TOC removal efficiency using the BiP-500 photocatalyst towards the photodegradation of RhB, OG and mixture dyes between two dyes (RhB-MB). After 12 min of irradiation, the removal of TOC from the photocatalytic reaction of RhB and OG reached about 82% and 63%, respectively. In other words, this photocatalyst can transform RhB and OG molecules, with relatively high efficiency, into CO_2 and H_2O, which can be crucial for water treatment. For the removal of dye mixtures, for example, in the case of RhB-MB, the analysis of total organic carbon shows catalytic degradation with an efficiency of 79.5% after 14 min of UV-Vis irradiation.

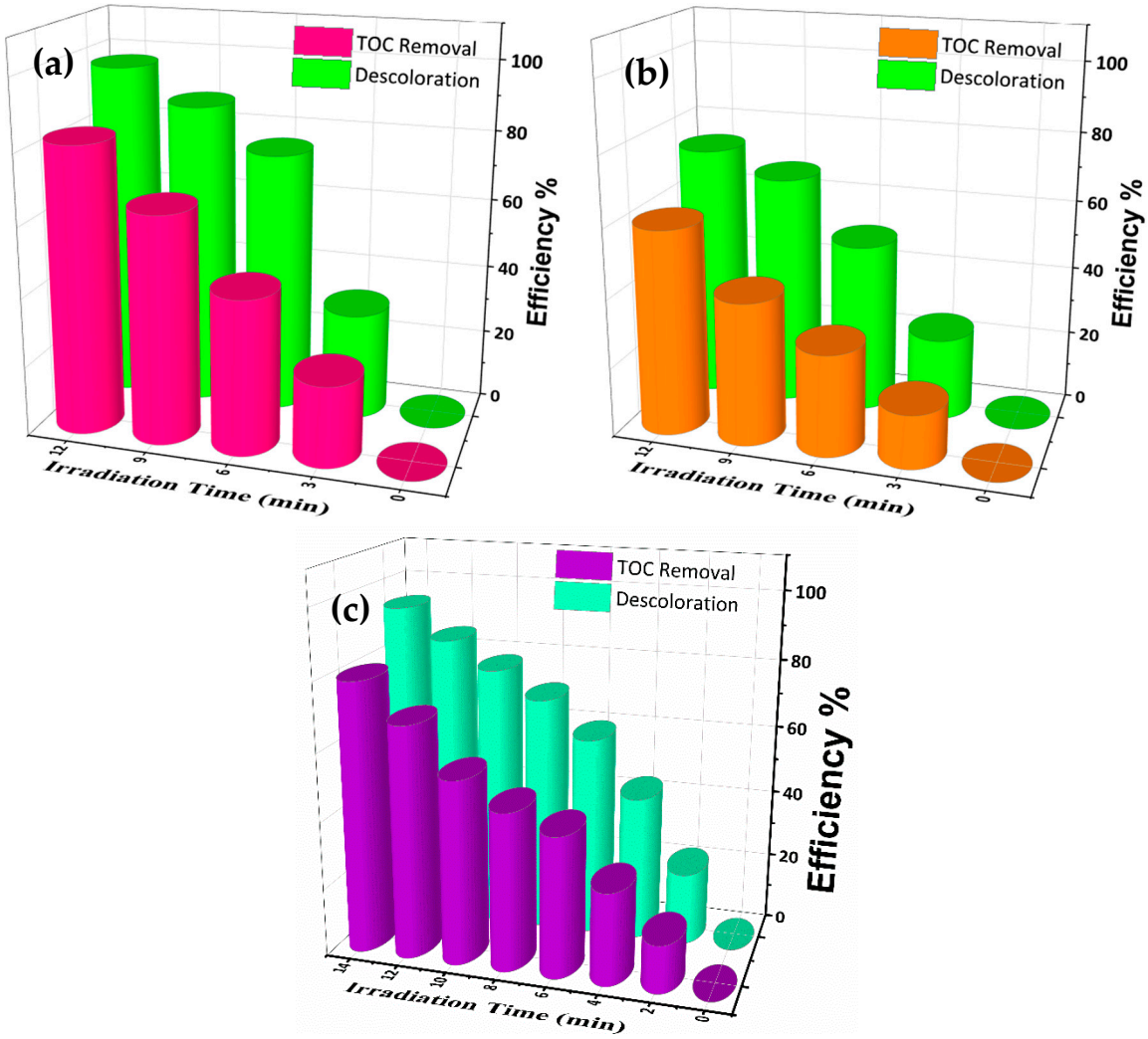

Figure 14. TOC removal and discoloration as a function of time of (**a**) Rhodamine B, (**b**) Orange G and (**c**) RhB-MB in the presence of the BiP-500 photocatalyst.

4.5. Role of Active Species

As we mentioned earlier, the degradation of Rhodamine B, for example, is complete after 12 min under UV-Vis irradiation at an initial concentration of 5 mg L^{-1}. To determine the photocatalytic mechanism through the identification of the main oxidative species, such as hydroxyl radical ($OH^{\bullet}$), hole (h^{+}) and superoxide radical ($O_2^{\bullet-}$), active species-trapping experiments were carried out. Isopropanol alcohol (IPA), disodium ethylenediaminetetraacetic acid (EDTA 2Na) and L-ascorbic acid were used as scavengers of ($OH^{\bullet}$) species, holes (h^{+}) and ($O_2^{\bullet-}$) species, respectively.

Figure 15a shows the effect of these scavengers on the photocatalytic efficiency of our BiP particles. We note that the photocatalytic degradation efficiency of RhB is 96.6% without scavengers. When IPA, EDTA-2Na and L-ascorbic acid are added, this efficiency decreases to 72.7%, 31.6%, and 12.8%, respectively. Thus, it could be inferred that h^{+} holes and $O_2^{\bullet-}$ ions should be the dominant active species in the photodegradation of Rhodamine B, while hydroxyl radicals ($OH^{\bullet}$) should play a minor role in the photocatalytic illumination. These results confirm what we found in our previous article [15]. From these results, the proposition of the photocatalytic degradation mechanism is given in Figure 15b.

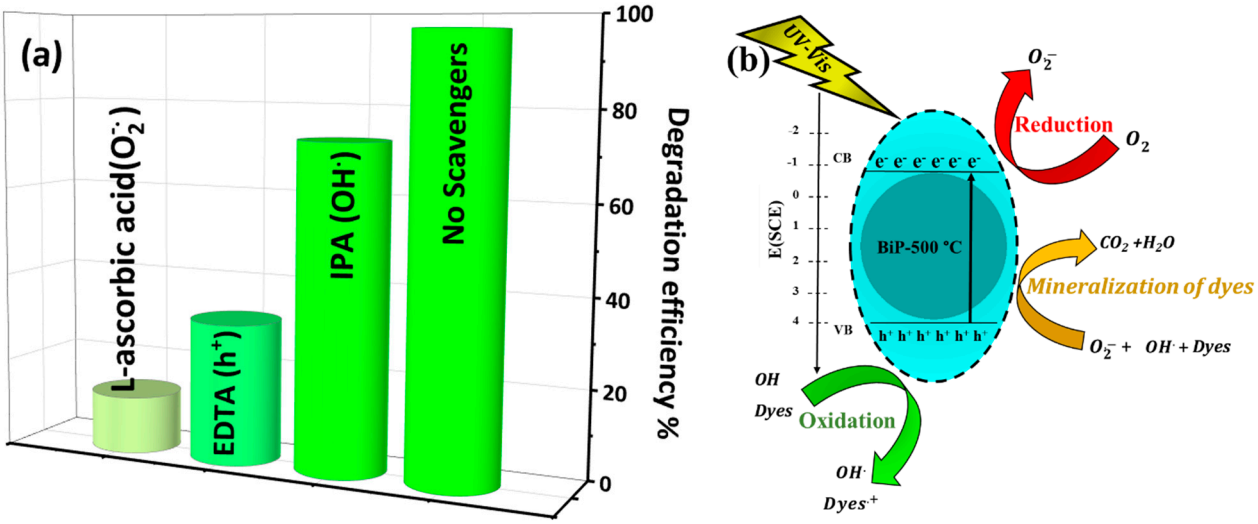

Figure 15. (**a**) Photocatalytic degradation of RhB using $BiPO_4$ in the presence of a series of scavengers. Irradiation time: 12 min, RhB = 5 mg L^{-1} and (scavenger) = 4 mmol L^{-1}. (**b**) Schematic diagram representing proposed degradation mechanism of BiP-500 °C.

4.6. Photodegradation of Parathion-Methyl (PM)

To confirm the performance of our BiP-500 photocatalyst, we studied its efficiency in the degradation of the pesticide parathion-methyl. The physicochemical properties [51] of parathion-methyl (PM) are presented in Table 4.

Table 4. Physicochemical properties of parathion-methyl [51].

Brute Formula	**C8H10NO5PS**
Chemical structure	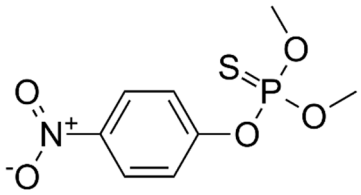
Chemical name	O,O-Dimethyl O-(p-nitrophenyl) phosphorothioate
Molecular mass	263.8 g/mol
Physical state	Crystallized solid
Water solubility	55 mg/L
Melting point	35–36 °C
λmax	278 nm

The UV-Vis absorbance measurements of parathion-methyl in the presence of the BiP-500 photocatalyst reveal that the intensity of the maximum absorption band, located at 278 nm, decreases as a function of time, and that its centroid shifts to longer wavelengths. Figure 16 shows the absorbance spectra of a PM solution, with a concentration of 10 ppm, in the presence of 100 mg of BiP-500 photocatalyst (BiP-500) = 1.0 g L^{-1}.

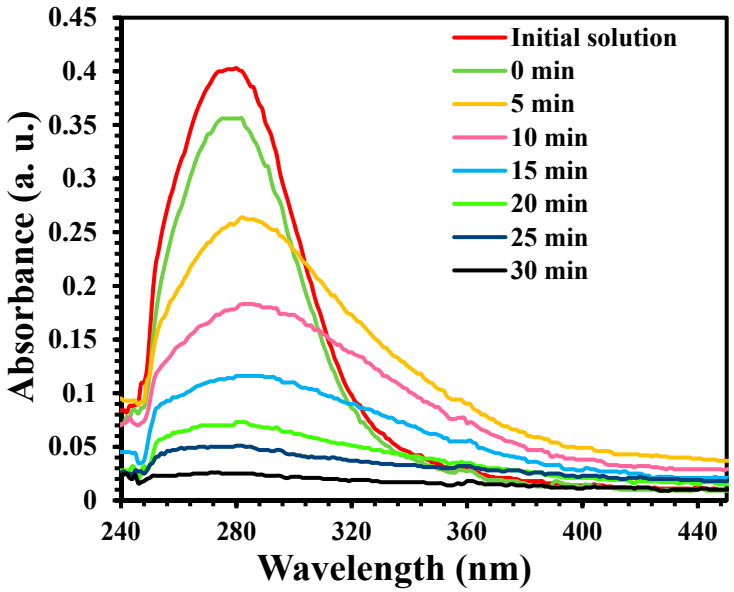

Figure 16. Evolution of the UV-Vis absorbance spectrum of parathion-methyl (PM = 10 mg L^{-1}).

We clearly observe a pronounced photodegradation of the PM until its total disappearance after 30 min of irradiation. We also observe a shift in the absorption maximum of the band from 278 nm to 283 nm associated with a modification of the absorption band profile. These modifications mainly occur during the first 5 min of irradiation under UV-Vis (254.3 nm) and reflect the appearance of degradation products.

5. Conclusions

In this study, bismuth phosphate $BiPO_4$ was obtained by a facile solid-state reaction at 500 °C. X-ray diffraction associated with Rietveld method calculations showed the presence of the unique polymorph $BiPO_4$ with space group $P2_1/n$. The polycrystalline material was characterized by a high degree of crystallization. The optical studies performed using DRS revealed an indirect band gap of 4.38 eV, which is in agreement with the value obtained using DFT. The BiP-500 photocatalyst was used to photodegrade six solutions of pollutants with variable performances decreasing from RhB to MO (RhB > MB > TB > CR > OG > MO). The point of zero charge study confirmed the affinity of the BiP-500 photocatalyst to degrade cationic dyes compared to anionic dyes. The photodegradation of mixtures of dyes and parathion-methyl as a toxic water pollutant in the agricultural sector completed the study, showing the capacity of BiP-500 particles to be used as photocatalysts for wastewater treatment.

Author Contributions: Data curation, B.A., E.A. and A.E.A.; Investigation, A.B. (Abdessalam Bouddouch); Methodology, A.B. (Abdessalam Bouddouch) and E.A.; Software, B.A. and A.E.A.; Supervision, B.B., S.V., F.G. and A.B. (Abdeljalil Benlhachemi); Writing—original draft, A.B. (Abdessalam Bouddouch); Writing—review and editing, B.A., B.B., A.T., S.V., F.G., J.-R.G. and A.B. (Abdeljalil Benlhachemi). All authors have read and agreed to the published version of the manuscript.

Funding: Financially supported by CAMPUS FRANCE (PHC TOUBKAL 2018 (France–Morocco bilateral program) Grant Number: 38999WE) and PPR project financed by the CNRST under number PPR/2015/32.

Data Availability Statement: Data is contained within the article.

Acknowledgments: This work was carried out in the laboratory materials and environment (LME), at the faculty of sciences Agadir, Ibn Zohr University, IM2NP laboratory, University of Toulon.

Conflicts of Interest: The authors declare that they have no known competing financial interest or personal relationships that could have appeared to influence the work reported in this paper.

References

1. Oliveira, T.P.; Rodrigues, S.F.; Marques, G.N.; Costa, R.C.V.; Lopes, C.G.G.; Aranas, C.; Rojas, A.; Rangel, J.H.G.; Oliveira, M.M. Synthesis, Characterization, and Photocatalytic Investigation of $CuFe_2O_4$ for the Degradation of Dyes under Visible Light. *Catalysts* **2022**, *12*, 623. [CrossRef]
2. Naciri, Y.; Hsini, A.; Ajmal, Z.; Bouddouch, A.; Bakiz, B.; Navío, J.; Albourine, A.; Valmalette, J.-C.; Ezahri, M.; Benlhachemi, A. Influence of Sr-doping on structural, optical and photocatalytic properties of synthesized $Ca_3(PO_4)_2$. *J. Colloid Interface Sci.* **2020**, *572*, 269–280. [CrossRef]
3. Chennah, A.; Naciri, Y.; Taoufyq, A.; Bakiz, B.; Bazzi, L.; Guinneton, F.; Villain, S.; Gavarri, J.R.; Benlhachemi, A. Electrodeposited zinc phosphate hydrate electrodes for electrocatalytic applications. *J. Appl. Electrochem.* **2018**, *49*, 163–177. [CrossRef]
4. Amaterz, E.; Tara, A.; Bouddouch, A.; Taoufyq, A.; Bakiz, B.; Benlhachemi, A.; Jbara, O. Photo-electrochemical degradation of wastewaters containing organics catalysed by phosphate-based materials: A review. *Rev. Environ. Sci. Bio/Technol.* **2020**, *19*, 843–872. [CrossRef]
5. Ellouzi, I.; Bouddouch, A.; Bakiz, B.; Benlhachemi, A.; Oualid, H.A. Glucose-assisted ball milling preparation of silver-doped biphasic TiO_2 for efficient photodegradation of Rhodamine B: Effect of silver-dopant loading. *Chem. Phys. Lett.* **2021**, *770*, 138456. [CrossRef]
6. Bouddouch, A.; Amaterz, E.; Bakiz, B.; Taoufyq, A.; Guinneton, F.; Villain, S.; Gavarri, J.-R.; Valmalette, J.-C.; Benlhachemi, A. Customized synthesis of functional bismuth phosphate using different methods: Photocatalytic and photoluminescence properties enhancement. *Nanotechnol. Environ. Eng.* **2021**, *6*, 4. [CrossRef]
7. Nethravathi, P.; Suresh, D. Silver-doped ZnO embedded reduced graphene oxide hybrid nanostructured composites for superior photocatalytic hydrogen generation, dye degradation, nitrite sensing and antioxidant activities. *Inorg. Chem. Commun.* **2021**, *134*, 109051. [CrossRef]
8. Naseeb, F.; Ali, N.; Khalil, A.; Khan, A.; Asiri, A.M.; Kamal, T.; Bakhsh, E.M.; Ul-Islam, M. Photocatalytic degradation of organic dyes by U_3MnO_{10} nanoparticles under UV and sunlight. *Inorg. Chem. Commun.* **2021**, *134*, 109075. [CrossRef]
9. Qi, S.; Zhang, R.; Zhang, Y.; Liu, X.; Xu, H. Preparation and photocatalytic properties of Bi_2WO_6/g-C_3N_4. *Inorg. Chem. Commun.* **2021**, *132*, 108761. [CrossRef]
10. Fu, H.; Pan, C.; Yao, A.W.; Zhu, Y. Visible-Light-Induced Degradation of Rhodamine B by Nanosized Bi_2WO_6. *J. Phys. Chem. B* **2005**, *109*, 22432–22439. [CrossRef]
11. Hoffmann, M.R.; Martin, S.T.; Choi, W.; Bahnemann, D.W. Environmental Applications of Semiconductor Photocatalysis. *Chem. Rev.* **1995**, *95*, 69–96. [CrossRef]
12. Pan, C.; Zhu, Y. New Type of $BiPO_4$ Oxy-Acid Salt Photocatalyst with High Photocatalytic Activity on Degradation of Dye. *Environ. Sci. Technol.* **2010**, *44*, 5570–5574. [CrossRef]
13. Pan, C.; Zhu, Y. A review of $BiPO_4$, a highly efficient oxyacid-type photocatalyst, used for environmental applications. *Catal. Sci. Technol.* **2015**, *5*, 3071–3083. [CrossRef]
14. Bouddouch, A.; Amaterz, E.; Bakiz, B.; Taoufyq, A.; Guinneton, F.; Villain, S.; Gavarri, J.; Ezahri, M.; Valmalette, J.; Benlhachemi, A. Role of thermal decomposition process in the photocatalytic or photoluminescence properties of $BiPO_4$ polymorphs. *Water Environ. Res.* **2020**, *92*, 1874–1887. [CrossRef]
15. Bouddouch, A.; Amaterz, E.; Bakiz, B.; Taoufyq, A.; Guinneton, F.; Villain, S.; Gavarri, J.-R.; Valmalette, J.-C.; Benlhachemi, A. Phase Transformation, Photocatalytic and Photoluminescent Properties of $BiPO_4$ Catalysts Prepared by Solid-State Reaction: Degradation of Rhodamine B. *Minerals* **2021**, *11*, 1007. [CrossRef]
16. Yang, S.; Xu, K.; Wang, H.; Yu, H.; Zhang, S.; Peng, F. Solution growth of peony-like copper hydroxyl-phosphate ($Cu_2(OH)PO_4$) flowers on Cu foil and their photocatalytic activity under visible light. *Mater. Des.* **2016**, *100*, 30–36. [CrossRef]
17. Ge, M. Photodegradation of rhodamine B and methyl orange by Ag_3PO_4 catalyst under visible light irradiation. *Chin. J. Catal.* **2014**, *35*, 1410–1417. [CrossRef]
18. Huang, H.; Chen, G.; Zhang, Y. Two Bi-based phosphate photocatalysts: Crystal structure, optical property and photocatalytic activity. *Inorg. Chem. Commun.* **2014**, *44*, 46–49. [CrossRef]
19. Bagtache, R.; Abdmeziem, K.; Rekhila, G.; Trari, M. Synthesis and semiconducting properties of Na_2MnPO_4F. Application to degradation of Rhodamine B under UV-light. *Mater. Sci. Semicond. Process.* **2016**, *51*, 1–7. [CrossRef]
20. Guo, J.; Zhang, J.; Chen, C.; Lan, Y. Rapid photodegradation of methyl orange by oxalic acid assisted with cathode material of lithium ion batteries $LiFePO_4$. *J. Taiwan Inst. Chem. Eng.* **2016**, *62*, 187–191. [CrossRef]
21. Liu, J.; Geng, B.; Wang, S. Preparation and Usage of ZnS/Phosphate Heterostructured Hemispheres in Enhanced Photocatalytic Activities. *Cryst. Growth Des.* **2009**, *9*, 4384–4390. [CrossRef]
22. Amaterz, E.; Tara, A.; Bouddouch, A.; Taoufyq, A.; Bakiz, B.; Lazar, F.; Gilliot, M.; Benlhachemi, A.; Bazzi, L.; Jbara, O. Hierarchical flower-like $SrHPO_4$ electrodes for the photoelectrochemical degradation of Rhodamine B. *J. Appl. Electrochem.* **2020**, *50*, 569–581. [CrossRef]
23. Amaterz, E.; Bouddouch, A.; Chennah, A.; Tara, A.; Taoufyq, A.; Bakiz, B.; Lazar, F.; Benlhachemi, A.; Bazzi, L.; Jbara, O. Heat treatment effect on the structure and morphology of strontium monoacid orthophosphate thin films. *Mater. Today Proc.* **2019**, *22*, 45–47. [CrossRef]
24. Amaterz, E.; Bouddouch, A.; Tara, A.; Taoufyq, A.; Bakiz, B.; Benlhachemi, A.; Jbara, O. Correlation between photoluminescence and photoelectrochemical properties of $SrHPO_4$/$BaHPO_4$/FTO anode material. *Opt. Mater.* **2020**, *109*, 110268. [CrossRef]

25. Akhsassi, B.; Bouddouch, A.; Naciri, Y.; Bakiz, B.; Taoufyq, A.; Favotto, C.; Villain, S.; Guinneton, F.; Benlhachemi, A. Enhanced photocatalytic activity of $Zn_3(PO_4)_2$/ZnO composite semiconductor prepared by different methods. *Chem. Phys. Lett.* **2021**, *783*, 139046. [CrossRef]
26. Liu, Y.; Zhu, Y.; Xu, J.; Bai, X.; Zong, R.; Zhu, Y. Degradation and mineralization mechanism of phenol by $BiPO_4$ photocatalysis assisted with H2O2. *Appl. Catal. B Environ.* **2013**, *142–143*, 561–567. [CrossRef]
27. Yang, Y.; Liu, B.; Zhang, Y.; Lv, X.; Wei, L.; Wang, X. Fabrication and luminescence of $BiPO_4$:Tb^{3+}/Ce^{3+} nanofibers by electrospinning. *Superlattices Microstruct.* **2016**, *90*, 227–235. [CrossRef]
28. Mooney-Slater, R.C.L. Polymorphic forms of bismuth phosphate. *Z. Kristallographie-Crystall. Mater.* **1962**, *117*, 371–385. [CrossRef]
29. Giannozzi, P.; Baroni, S.; Bonini, N.; Calandra, M.; Car, R.; Cavazzoni, C.; Ceresoli, D.; Chiarotti, G.L.; Cococcioni, M.; Dabo, I.; et al. QUANTUM ESPRESSO: A modular and open-source software project for quantum simulations of materials. *J. Phys. Condens. Matter* **2009**, *21*, 395502. [CrossRef]
30. Perdew, J.P.; Burke, K.; Ernzerhof, M. Generalized gradient approximation made simple. *Phys. Rev. Lett.* **1996**, *77*, 3865. [CrossRef]
31. Monkhorst, H.J.; Pack, J.D. Special points for Brillouin-zone integrations. *Phys. Rev. B* **1976**, *13*, 5188. [CrossRef]
32. Al-Harahsheh, M.; Shawabkeh, R.; Al-Harahsheh, A.; Tarawneh, K.; Batiha, M.M. Surface modification and characterization of Jordanian kaolinite: Application for lead removal from aqueous solutions. *Appl. Surf. Sci.* **2009**, *255*, 8098–8103. [CrossRef]
33. Rodriguez-Carvajal, J. Roisnel, FullProf. 98 and WinPLOTR: New windows 95/NT applications for diffraction commission for powder diffraction. *Int. Union Crystallogr. Newsl.* **1998**, *20*, 35–36.
34. Romero, B.; Bruque, S.; Aranda, M.A.G.; Iglesias, J.E. Syntheses, Crystal Structures, and Characterization of Bismuth Phosphates. *Inorg. Chem.* **1994**, *33*, 1869–1874. [CrossRef]
35. Bérar, J.-F.; Lelann, P. ESD's and estimated probable error obtained in Rietveld refinements with local correlations. *J. Appl. Crystallogr.* **1991**, *24*, 1–5. [CrossRef]
36. Vadivel, S.; Maruthamani, D.; Kumaravel, M.; Saravanakumar, B.; Paul, B.; Dhar, S.S.; Muthuraj, V. Supercapacitors studies on $BiPO_4$ nanoparticles synthesized via a simple microwave approach. *J. Taibah Univ. Sci.* **2017**, *11*, 661–666. [CrossRef]
37. Zhao, M.; Li, G.; Zheng, J.; Li, L.; Wang, H.; Yang, L. Preparation and polymorph-sensitive luminescence properties of $BiPO_4$:Eu, Part I: Room-temperature reaction followed by a heat treatment. *CrystEngComm* **2011**, *13*, 6251–6257. [CrossRef]
38. Zhao, M.; Li, L.; Yang, L.; Zheng, J.; Li, G. Exploring the unique electrical properties of metastable $BiPO_4$ through switchable phase transitions. *CrystEngComm* **2013**, *15*, 609–615. [CrossRef]
39. Zhu, Z.; Zhang, K.; Zhao, H.; Zhu, J. UV-light driven photocatalytic performance of hydrothermally-synthesized hexagonal $CePO_4$ nanorods. *Solid State Sci.* **2017**, *72*, 28–32. [CrossRef]
40. Tauc, J.; Grigorovici, R.; Vancu, A. Optical Properties and Electronic Structure of Amorphous Germanium. *Phys. Status Solidi B* **1966**, *15*, 627–637. [CrossRef]
41. Wu, Z.; Liu, J.; Tian, Q.; Wu, W. Efficient Visible Light Formaldehyde Oxidation with 2D *p-n* Heterostructure of BiOBr/$BiPO_4$ Nanosheets at Room Temperature. *ACS Sustain. Chem. Eng.* **2017**, *5*, 5008–5017. [CrossRef]
42. Hizhnyi, Y.A.; Nedilko, S.; Chornii, V.; Slobodyanik, M.; Zatovsky, I.; Terebilenko, K. Electronic structures and origin of intrinsic luminescence in Bi-containing oxide crystals $BiPO_4$, $K_3Bi_5(PO_4)_6$, $K_2Bi(PO_4)(MoO_4)$, $K_2Bi(PO_4)(WO_4)$ and $K_5Bi(MoO_4)_4$. *J. Alloys Compd.* **2014**, *614*, 420–435. [CrossRef]
43. Al-Ghouti, M.; Khraisheh, M.; Allen, S.; Ahmad, M. The removal of dyes from textile wastewater: A study of the physical characteristics and adsorption mechanisms of diatomaceous earth. *J. Environ. Manag.* **2003**, *69*, 229–238. [CrossRef] [PubMed]
44. Schwarz, J.; Driscoll, C.T.; Bhanot, A. The zero point of charge of silica—Alumina oxide suspensions. *J. Colloid Interface Sci.* **1984**, *97*, 55–61. [CrossRef]
45. Milonjić, S.K.; Kopečni, M.M.; Ilić, Z.E. The point of zero charge and adsorption properties of natural magnetite. *J. Radioanal. Nucl. Chem.* **1983**, *78*, 15–24. [CrossRef]
46. Pan, C.; Xu, J.; Chen, Y.; Zhu, Y. Influence of OH-related defects on the performances of $BiPO_4$ photocatalyst for the degradation of rhodamine B. *Appl. Catal. B Environ.* **2012**, *115–116*, 314–319. [CrossRef]
47. Becerro, A.I.; Criado, J.; Gontard, L.C.; Obregón, S.; Fernández, A.; Colón, G.; Ocaña, M. Bifunctional, Monodisperse $BiPO_4$-Based Nanostars: Photocatalytic Activity and Luminescent Applications. *Cryst. Growth Des.* **2014**, *14*, 3319–3326. [CrossRef]
48. Li, G.; Ding, Y.; Zhang, Y.; Lu, Z.; Sun, H.; Chen, R. Microwave synthesis of $BiPO_4$ nanostructures and their morphology-dependent photocatalytic performances. *J. Colloid Interface Sci.* **2011**, *363*, 497–503. [CrossRef]
49. Zhu, Y.; Liu, Y.; Lv, Y.; Ling, Q.; Liu, D.; Zhu, Y. Enhancement of photocatalytic activity for $BiPO_4$via phase junction. *J. Mater. Chem. A* **2014**, *2*, 13041–13048. [CrossRef]
50. Yan-Yan, Z.; Yan-Fang, L.; Yan-Hui, L.; Hua, W.; Qiang, L.; Yong-Fa, Z. Reflux Preparation and Photocatalytic Performance of Bismuth Phosphate Nanorods. *Acta Phys.-Chim. Sin.* **2013**, *29*, 576–584. [CrossRef]
51. Zangiabadi, M.; Mehrabi, F.; Nasiripur, P.; Baghersad, M.H. Visible-light-driven photocatalytic degradation of methyl parathion as chemical warfare agent simulant by NiO/Bi_2MoO_6 heterojunction photocatalyst. *J. Mol. Struct.* **2022**, *1256*, 132472. [CrossRef]